T cell migration requires ion and water influx to regulate actin polymerization

Authors:
Leonard L. de Boer[1,2], Serena Melgrati[1,2], Lesley Vanes[1], Joshua Biggs O'May[1], Darryl Hayward[1], Robert Köchl[1], Victor L. J. Tybulewicz[1,2]

Affiliations:
[1]The Francis Crick Institute, London, NW1 1AT, UK
[2]Imperial College, London W12 0NN, UK

*Correspondence to:

Victor L. J. Tybulewicz
The Francis Crick Institute,
1 Midland Road,
London, NW1 1AT, UK

Tel: +44 20 3796 1612
Email: Victor.T@crick.ac.uk

Present addresses:

SM: Institute for Research in Biomedicine, Università della Svizzera Italiana, Bellinzona, Switzerland.
RK: Kings College London, London, SE1 9RT, UK
DH: GSK, Stevenage, SG1 2NY, UK

Abstract:

Migration of T cells is essential for their ability to mount immune responses. Chemokine-induced T cell migration requires WNK1, a kinase that regulates ion influx into the cell. However, it is not known why ion entry is necessary for T cell movement. We show that signaling from the chemokine receptor CCR7 leads to activation of WNK1 and its downstream pathway at the leading edge of migrating $CD4^+$ T cells, leading to ion influx and consequent water entry by osmosis through AQP3. This WNK1-induced water entry is required to swell the membrane at the leading edge, generating space into which actin filaments can polymerize, thereby facilitating forward movement of the cell.

One Sentence Summary:

Chemokine-induced migration of T cells requires water entry at the leading edge to facilitate actin polymerization.

Main text:

Naive T cells migrate between lymphoid organs in search of antigen, a process that is essential for adaptive immune responses (*1*). T cells exit the bloodstream in response to CCL21 chemokine signaling via CCR7 leading to integrin-dependent adhesion to endothelium and migration through it. Once inside lymph node parenchyma, T cells migrate rapidly in response to CCR7 signals, now using an integrin-independent mode of migration to scan antigen-presenting cells for the presence of cognate antigen.

WNK1 is a member of the WNK-family of serine/threonine protein kinases that regulate ion homeostasis in kidney epithelial cells where they promote uptake of Na^+, K^+ and Cl^- ions from urine (*2*). When activated, WNK1 phosphorylates and activates two related kinases OXSR1 and STK39, which in turn phosphorylate members of the

SLC12A-family of ion co-transporters altering their activity, resulting in a net influx of ions (*3*).

We previously demonstrated that WNK1, the only WNK-family member expressed in T cells, is required for their chemokine-induced migration (*4*). We showed that stimulation of $CD4^+$ T cells with CCL21 results in rapid phosphorylation of OXSR1, indicating that CCR7 transduces signals leading to WNK1 activation. Furthermore, CCL21-induced migration was partially inhibited in $CD4^+$ T cells with mutations in *Oxsr1* and SLC12A2 or treated with bumetanide (SLC12A2i), an SLC12A2 inhibitor (*4*). Taken together, these results lead to the surprising conclusion that CCR7 signaling via WNK1 results in ion influx via SLC12A2 which is required for T cell migration. Thus, a pathway regulating ion homeostasis plays a critical role in T cell movement. However, it remains unclear why ion influx is required for this process.

To understand how WNK1 pathway-regulated ion influx contributes to migration, we analyzed the functional requirement for the pathway proteins in T cells migrating in confinement, to model their migration within lymphoid tissue. Furthermore, we evaluated the sub-cellular distribution of the WNK pathway proteins and their activities under the same conditions. Using tamoxifen-inducible ablation of *Wnk1*, we generated WNK1-expressing (*Wnk1*$^{+/-}$RCE) and WNK1-deficient (*Wnk1*$^{-/-}$RCE) $CD4^+$ T cells (see Methods), and imaged their CCL21-induced migration under agarose on ICAM-1. We found that in the absence of WNK1, T cells migrated more slowly (Video S1, Fig. S1A-B, Fig. 1A). Using a similar tamoxifen-inducible ablation of *Oxsr1*, we found that $CD4^+$ T cells deficient in OXSR1 and expressing a mutant STK39-T243A that cannot be phosphorylated and activated by WNK1 (*5*) (*Oxsr1*$^{-/-}$*Stk39*$^{T243A/T243A}$RCE) also migrated more slowly (Fig. 1B).

To extend this, we used inhibitors against WNK1 pathway proteins. WNK463 (WNKi), a selective WNK inhibitor (*6*), completely blocked CCL21-induced phosphorylation of OXSR1 on S325, a known target of WNK1 activity (*7*) (Fig. S1C). WNKi showed a dose-dependent inhibition of CCL21-induced migration speed and shape polarization (Fig. S1D, Fig. 1C). Furthermore, treatment of T cells with SLC12A2i also caused a decrease in migration speed (Fig. 1D), although the effect was smaller than with WNKi, potentially due to redundancy between SLC12A-family ion co-transporters, four of which are expressed in T cells. Similar results were observed in $CD4^+$ T cells migrating in 3D in a collagen-I matrix (Video S2, Fig. S1E-G). Taken together, these results show that WNK1, OXSR1, STK39 and ion influx through SLC12A2 are required for CCL21-induced migration of T cells in confinement.

Live cell imaging of T cells expressing GFP-tagged WNK1, OXSR1 and SLC12A2 migrating in response to CCL21 showed that all three proteins were more abundant at the leading edge of the cell compared to the distribution of GFP only (Video S3, Fig. 2A-C). Furthermore, imaging of fixed cells demonstrated that in migrating T cells, WNK1, OXSR1 and SLC12A2 are enriched at the leading edge and depleted at the trailing edge as identified by localization of CDC42 and CD44, respectively (Fig. 2D-E, S2A-B). To analyze activity of the pathway we imaged the distribution of phosphorylated WNK1 (S382), OXSR1 (S325), and SLC12A2 (T203/T207/T212), phosphorylations that indicate increased activity of these proteins (*7-9*). Notably, these phospho-proteins were also enriched at the leading edge of the migrating T cells (Fig. 2D-E, S2A-B). Thus, in T cells migrating in response to CCL21, WNK1 pathway proteins and their activities accumulate at the leading edge of the cell, implying that CCR7 signaling via WNK1, OXSR1 and STK39 leads to localized entry of Na^+, K^+ and Cl^- ions via SLC12A2 at the leading edge of migrating T cells.

WNK1-induced ion influx would be predicted to cause water entry by osmosis. In support of this, WNK1 has been shown to regulate the volume of non-lymphoid cells, allowing rapid responses to changing extracellular osmolarity by controlling movement of ions and hence water across the plasma membrane (*10*). Thus, we hypothesized that WNK1-mediated ion influx would cause water entry, which would be required for migration. To determine if the WNK1 pathway regulates water movement in $CD4^+$ T cells, we measured the volume of cells with defects in the pathway. CCL21 induced a volume increase in WNK1-expressing T cells, whereas no such increase was seen in the absence of WNK1, or if WNK1 was inhibited (Fig. 1E-F). Furthermore, WNK1-deficient or WNK1-inhibited T cells were about 15% smaller even in the absence of CCL21, indicating a basal homeostatic function for WNK1 in regulating cell volume. Mutation of *Oxsr1* and *Stk39* also caused T cells to become smaller and to no longer respond to CCL21 by increasing in volume (Fig. 1G). In contrast, SLC12A2i did not change basal T cell volume but blocked the CCL21-induced volume increase (Fig. 1H), consistent with this inhibitor having the smallest effect on migration speed (Fig. 1D). Thus WNK1, OXSR1, STK39 and SLC12A2 regulate the volume of T cells, supporting the hypothesis that WNK1 pathway activity results in water influx which is required for volume regulation.

Water enters cells through aquaporin (AQP) channels, of which $CD4^+$ T cells predominantly express AQP3 (www.immgen.org). To investigate the importance of water movement for T cell migration we used DFP00173 (AQP3i), a selective AQP3 inhibitor (*11*). Notably, AQP3i caused a significant decrease in the speed of CCL21-induced migration of T cells under agarose or in a collagen-I matrix, in agreement with previous studies of AQP3-deficient T cells (*12*) (Fig. 1D, S1G). Measurement of cell volume showed that like SLC12A2i, AQP3i did not change the basal volume of T cells but eliminated the CCL21-induced volume increase (Fig. 1H). Furthermore, AQP3 is localized to the leading edge of migrating T cells (Fig. 2D-E, S2A-B). Thus, AQP3 is

required for CCL21-induced water entry and migration in $CD4^+$ T cells, supporting the hypothesis that localized water entry is required for T cell migration.

Migration of T cells requires actin polymerization at the leading edge which results in F-actin filaments pushing forward against the plasma membrane (*13, 14*). To determine if this process may be controlled by the WNK1 pathway, we measured total F-actin in CCL21-stimulated $CD4^+$ T cells using flow cytometry. This showed a rapid CCL21-induced increase in F-actin which was partially decreased by inhibition of WNK1 and SLC12A2 and by *Oxsr1* and *Stk39* mutations (Fig. S3A-C), implying that the WNK1 pathway and ion influx may regulate actin polymerization.

Forward protrusion of actin filaments at the leading edge is generated by G-actin monomer addition to F-actin filament tips through a mechanism known as the Brownian ratchet model (*15-17*). Thermal (Brownian) motion of both the membrane and the filaments results in a fluctuating gap, and when this exceeds 2.7 nm, an actin monomer can be added to the filament tip, thereby extending it. This prevents the membrane from returning to its original position, resulting in incremental forward protrusion. We hypothesized that WNK1-induced water entry at the leading edge would result in localized swelling of the membrane, pulling it away from underlying F-actin, thereby creating space into which actin filaments can polymerize, a mechanism we term a facilitated Brownian ratchet. To directly test if the WNK1-induced water movement affects spacing between the plasma membrane and the underlying F-actin, we used instant structured illumination microscopy, a super-resolution method, to image the plasma membrane and F-actin in $CD4^+$ T cells migrating in response to CCL21 (*18*). We found that at the leading edge the distance from the plasma membrane to the peak F-actin signal was around 174 nm, whereas at the side of the cell, this distance was around 43 nm, consistent with an increased spacing at the leading edge, a requirement for forward protrusion of actin filaments (Fig.3A-B). Notably, treatment of the T cells

with SLC12A2i or AQP3i caused a significant decrease in the membrane to F-actin spacing, with AQP3i again having the stronger effect (Video S4, Fig. 3C-D). Importantly, we noted a significant correlation between membrane-F-actin spacing and cell speed, supporting our hypothesis that this spacing is critical for T cell migration (Fig. 3E). Thus, ion and water influx are required to maintain a larger membrane to peak F-actin spacing at the leading edge.

Analysis of F-actin in migrating cells has shown that despite greatly elevated levels of F-actin at the front of the cell, there is a lower density of membrane-proximal actin (MPA) at the leading edge compared to other parts of the migrating cell (*19*). We hypothesized that WNK1-induced water entry and membrane swelling may contribute to the reduced MPA at the leading edge. To test this, we analyzed migrating T cells expressing two fluorescent probes: MPAct-mCherry (MPAct) and GFP-CaaX (CaaX) (*19*). Both contain fluorescent proteins that are tethered to the plasma membrane, but MPAct also contains an F-actin-binding domain. Thus, CaaX is evenly distributed on the plasma membrane, whereas MPAct accumulates in regions of the membrane with higher concentrations of underlying MPA that is within 10 nm of the membrane. Hence the MPAct/CaaX ratio is a measure of the distribution of MPA. Analysis of T cells expressing MPAct and CaaX, migrating in response to CCL21, showed that, as expected the MPAct/CaaX ratio is reduced in the leading edge compared to the side and trailing edges (Fig. 4A-B). Notably, treatment of T cells with SLC12A2i or AQP3i resulted in a significant increase in MPA at the leading edge, with less polarization of the MPA signal between the front and back of the cell (Video S5, Fig. S3D-E, 4C-E). Thus, ion and water influx are required to maintain reduced MPA at the leading edge of T cells, consistent with our hypothesis that water entry causes the membrane to swell away from the underlying F-actin.

If WNK1-induced water entry at the leading edge is required to generate space and hence facilitate the Brownian ratchet mechanism of actin filament growth, inhibition of the pathway should affect the rate of actin polymerization at the membrane. Continuous addition of G-actin monomers at the leading edge of migrating cells results in retrograde flow of F-actin, which can thus be used as a surrogate for actin addition at the front of the cell (*20*). To determine if the WNK1 pathway regulates this process, we measured rates of retrograde actin flow in CCL21-stimulated T cells expressing LifeAct-eGFP to visualize F-actin. In contrast to a partial decrease in total F-actin, retrograde actin flow was strongly decreased in WNK1-deficient or WNK1-inhibited T cells (Video S6, Fig. S3F-G, 4F-G). Furthermore, both SLC12A2i and AQP3i partially inhibited retrograde actin flow, with the AQP3i having the stronger effect. Thus, WNK1 and ion and water influx are required for actin retrograde flow, consistent with our hypothesis that they influence the rate of addition of G-actin monomers to the growing tips of F-actin filaments at the leading edge.

To directly determine if WNK1-induced water entry is required for migration, we asked if forcing water into the cells by reducing the tonicity of the medium could rescue migration in WNK1-inhibited cells. Remarkably, while reducing tonicity caused a reduction of migration speed in T cells treated with vehicle control, it increased migration speed in cells where WNK1 had been partially inhibited. This was most effective at 248 mOsm/l, a ~15% reduction of tonicity compared to isotonic medium (292 mOsm/l) (Fig. 4H). The hypotonic rescue of migration in WNK1-inihibited T cells could be due to the increased water entry, or, alternatively, a result of reduced NaCl concentration. To distinguish these possibilities, we compared the migration speed of WNK1-inhibited T cells in hypotonic medium at 248 mOsm/l or in isotonic medium with the same reduced amount of NaCl but with isotonic osmolarity restored using L-glucose, an inert osmolyte (Fig 4I). Whereas hypotonic medium rescued most of the migration defect of WNK1-inhibited cells, isotonic medium with reduced NaCl was

much less effective, demonstrating that water entry is required for T cell migration. Furthermore, analysis of retrograde actin flow in WNK1-inhibited T cells, showed that this too was partially rescued when the cells were placed in hypotonic medium (Fig. 4J). Thus, WNK1-induced water entry is required for CCL21-induced actin flow and T cell migration.

The importance of membrane protrusion for forward actin polymerization at the leading edge is supported by studies showing that increased load on lamellipodial F-actin results in a dense actin network with many filaments growing at shallow angles to the membrane (*21, 22*). In contrast, decreased load results in increased polymerization of actin filaments perpendicular to the membrane, causing rapid forward protrusion of the leading edge. Our studies provide a mechanism by which such reduced force is achieved. We demonstrate that CCR7 signaling at the leading edge of T cells results in localized activation of the WNK1 pathway causing water entry and membrane swelling. This would be predicted to decrease the force on the underlying F-actin network and thereby facilitate forward growth of actin filaments. Given the broad expression of WNK1 (*23*), similar pathways may play important roles in the migration of many cell types both within the immune system and beyond it. Indeed, previous studies had shown that inhibition of the sodium-hydrogen exchanger NHE-1 (SLC9A1) or AQP9 decreases fMLP-induced migration of human neutrophils, and SLC12A2 inhibition reduces migration of glioblastoma cells, indicating that ion and water movement may be important for migration (*24-26*). However, the mechanistic basis of these observations was unclear. Our results provide an explanation for why ion and water movement are likely to be important for cell migration in multiple cell types including metastatic tumor cells.

In summary, our results show that CCL21 binding to CCR7 on $CD4^+$ T cells causes signaling at the leading edge via WNK1, OXSR1 and STK39 to SLC12A2 and

potentially other SLC12A-family ion co-transporters, resulting in ion influx, which in turn drives water entry via AQP3 (Fig. 4K). This water entry is required to cause swelling of the plasma membrane, allowing it to move away from the underlying F-actin, thereby generating space into which actin filaments can extend, facilitating a Brownian ratchet mechanism that is essential for forward cell movement.

References:

1. J. P. Girard, C. Moussion, R. Forster, HEVs, lymphatics and homeostatic immune cell trafficking in lymph nodes. *Nat Rev Immunol* **12**, 762-73 (2012).
2. M. Shekarabi, J. Zhang, A. R. Khanna, D. H. Ellison, E. Delpire, K. T. Kahle, WNK Kinase Signaling in Ion Homeostasis and Human Disease. *Cell Metab* **25**, 285-299 (2017).
3. D. R. Alessi, J. Zhang, A. Khanna, T. Hochdorfer, Y. Shang, K. T. Kahle, The WNK-SPAK/OSR1 pathway: master regulator of cation-chloride cotransporters. *Sci Signal* **7**, re3 (2014).
4. R. Köchl, F. Thelen, L. Vanes, T. F. Brazao, K. Fountain, J. Xie, C. L. Huang, R. Lyck, J. V. Stein, V. L. Tybulewicz, WNK1 kinase balances T cell adhesion versus migration in vivo. *Nat Immunol* **17**, 1075-83 (2016).
5. F. H. Rafiqi, A. M. Zuber, M. Glover, C. Richardson, S. Fleming, S. Jovanovic, A. Jovanovic, K. M. O'Shaughnessy, D. R. Alessi, Role of the WNK-activated SPAK kinase in regulating blood pressure. *EMBO Mol Med* **2**, 63-75 (2010).
6. K. Yamada, H. M. Park, D. F. Rigel, K. DiPetrillo, E. J. Whalen, A. Anisowicz, M. Beil, J. Berstler, C. E. Brocklehurst, D. A. Burdick, S. L. Caplan, M. P. Capparelli, G. Chen, W. Chen, B. Dale, L. Deng, F. Fu, N. Hamamatsu, K. Harasaki, T. Herr, P. Hoffmann, Q. Y. Hu, W. J. Huang, N. Idamakanti, H. Imase, Y. Iwaki, M. Jain, J. Jeyaseelan, M. Kato, V. K. Kaushik, D. Kohls, V. Kunjathoor, D. LaSala, J. Lee, J. Liu, Y. Luo, F. Ma, R. Mo, S. Mowbray, M. Mogi, F. Ossola, P. Pandey, S. J. Patel, S. Raghavan, B. Salem, Y. H. Shanado, G. M. Trakshel, G. Turner, H. Wakai, C. Wang, S. Weldon, J. B. Wielicki, X. Xie, L. Xu, Y. I. Yagi, K. Yasoshima, J. Yin, D. Yowe, J. H. Zhang, G. Zheng, L. Monovich, Small-molecule WNK inhibition regulates cardiovascular and renal function. *Nat Chem Biol* **12**, 896-898 (2016).

7. A. C. Vitari, M. Deak, N. A. Morrice, D. R. Alessi, The WNK1 and WNK4 protein kinases that are mutated in Gordon's hypertension syndrome phosphorylate and activate SPAK and OSR1 protein kinases. *Biochem. J.* **391**, 17-24 (2005).

8. A. C. Vitari, J. Thastrup, F. H. Rafiqi, M. Deak, N. A. Morrice, H. K. Karlsson, D. R. Alessi, Functional interactions of the SPAK/OSR1 kinases with their upstream activator WNK1 and downstream substrate NKCC1. *Biochem. J.* **397**, 223-31 (2006).

9. A. Zagórska, E. Pozo-Guisado, J. Boudeau, A. C. Vitari, F. H. Rafiqi, J. Thastrup, M. Deak, D. G. Campbell, N. A. Morrice, A. R. Prescott, D. R. Alessi, Regulation of activity and localization of the WNK1 protein kinase by hyperosmotic stress. *J Cell Biol* **176**, 89-100 (2007).

10. P. de Los Heros, D. Pacheco-Alvarez, G. Gamba, Role of WNK Kinases in the Modulation of Cell Volume. *Curr. Top. Membr.* **81**, 207-235 (2018).

11. Y. Sonntag, P. Gena, A. Maggio, T. Singh, I. Artner, M. K. Oklinski, U. Johanson, P. Kjellbom, J. D. Nieland, S. Nielsen, G. Calamita, M. Rutzler, Identification and characterization of potent and selective aquaporin-3 and aquaporin-7 inhibitors. *J Biol Chem* **294**, 7377-7387 (2019).

12. M. Hara-Chikuma, S. Chikuma, Y. Sugiyama, K. Kabashima, A. S. Verkman, S. Inoue, Y. Miyachi, Chemokine-dependent T cell migration requires aquaporin-3-mediated hydrogen peroxide uptake. *J Exp Med* **209**, 1743-52 (2012).

13. L. Dupre, R. Houmadi, C. Tang, J. Rey-Barroso, T Lymphocyte Migration: An Action Movie Starring the Actin and Associated Actors. *Front Immunol* **6**, 586 (2015).

14. D. L. Bodor, W. Ponisch, R. G. Endres, E. K. Paluch, Of Cell Shapes and Motion: The Physical Basis of Animal Cell Migration. *Dev Cell* **52**, 550-562 (2020).

15. C. S. Peskin, G. M. Odell, G. F. Oster, Cellular motions and thermal fluctuations: the Brownian ratchet. *Biophysical Journal* **65**, 316-324 (1993).

16. J. Funk, F. Merino, M. Schaks, K. Rottner, S. Raunser, P. Bieling, A barbed end interference mechanism reveals how capping protein promotes nucleation in branched actin networks. *Nat Commun* **12**, 5329 (2021).

17. D. Holz, D. Vavylonis, Building a dendritic actin filament network branch by branch: models of filament orientation pattern and force generation in lamellipodia. *Biophys Rev* **10**, 1577-1585 (2018).

18. M. P. Clausen, H. Colin-York, F. Schneider, C. Eggeling, M. Fritzsche, Dissecting the actin cortex density and membrane-cortex distance in living cells by super-resolution microscopy. *J Phys D Appl Phys* **50**, 064002 (2017).

19. A. Bisaria, A. Hayer, D. Garbett, D. Cohen, T. Meyer, Membrane-proximal F-actin restricts local membrane protrusions and directs cell migration. *Science* **368**, 1205-1210 (2020).

20. J. Renkawitz, K. Schumann, M. Weber, T. Lammermann, H. Pflicke, M. Piel, J. Polleux, J. P. Spatz, M. Sixt, Adaptive force transmission in amoeboid cell migration. *Nat Cell Biol* **11**, 1438-43 (2009).

21. P. Bieling, T. D. Li, J. Weichsel, R. McGorty, P. Jreij, B. Huang, D. A. Fletcher, R. D. Mullins, Force Feedback Controls Motor Activity and Mechanical Properties of Self-Assembling Branched Actin Networks. *Cell* **164**, 115-127 (2016).

22. J. Mueller, G. Szep, M. Nemethova, I. de Vries, A. D. Lieber, C. Winkler, K. Kruse, J. V. Small, C. Schmeiser, K. Keren, R. Hauschild, M. Sixt, Load Adaptation of Lamellipodial Actin Networks. *Cell* **171**, 188-200 e16 (2017).

23. M. Shekarabi, R. G. Lafreniere, R. Gaudet, J. Laganiere, M. M. Marcinkiewicz, P. A. Dion, G. A. Rouleau, Comparative analysis of the expression profile of Wnk1 and Wnk1/Hsn2 splice variants in developing and adult mouse tissues. *PLoS One* **8**, e57807 (2013).

24. M. Ritter, P. Schratzberger, H. Rossmann, E. Woll, K. Seiler, U. Seidler, N. Reinisch, C. M. Kahler, H. Zwierzina, H. J. Lang, F. Lang, M. Paulmichl, C. J. Wiedermann, Effect of inhibitors of Na+/H+-exchange and gastric H+/K+ ATPase on cell volume, intracellular pH and migration of human polymorphonuclear leucocytes. *Br J Pharmacol* **124**, 627-38 (1998).

25. V. M. Loitto, T. Forslund, T. Sundqvist, K. E. Magnusson, M. Gustafsson, Neutrophil leukocyte motility requires directed water influx. *J Leukoc Biol* **71**, 212-22 (2002).

26. T. Garzon-Muvdi, P. Schiapparelli, C. ap Rhys, H. Guerrero-Cazares, C. Smith, D. H. Kim, L. Kone, H. Farber, D. Y. Lee, S. S. An, A. Levchenko, A. Quinones-Hinojosa, Regulation of brain tumor dispersal by NKCC1 through a novel role in focal adhesion regulation. *PLoS Biol* **10**, e1001320 (2012).

27. J. Xie, T. Wu, K. Xu, I. K. Huang, O. Cleaver, C. L. Huang, Endothelial-specific expression of WNK1 kinase is essential for angiogenesis and heart development in mice. *Am J Pathol* **175**, 1315-27 (2009).

28. S. H. Lin, I. S. Yu, S. T. Jiang, S. W. Lin, P. Chu, A. Chen, H. K. Sytwu, E. Sohara, S. Uchida, S. Sasaki, S. S. Yang, Impaired phosphorylation of Na(+)-K(+)-2Cl(-) cotransporter by oxidative stress-responsive kinase-1 deficiency manifests hypotension and Bartter-like syndrome. *Proc Natl Acad Sci U S A* **108**, 17538-43 (2011).

29. C. de Luca, T. J. Kowalski, Y. Zhang, J. K. Elmquist, C. Lee, M. W. Kilimann, T. Ludwig, S. M. Liu, S. C. Chua, Jr., Complete rescue of obesity, diabetes, and infertility in db/db mice by neuron-specific LEPR-B transgenes. *J Clin Invest* **115**, 3484-93 (2005).

30. J. Riedl, K. C. Flynn, A. Raducanu, F. Gartner, G. Beck, M. Bosl, F. Bradke, S. Massberg, A. Aszodi, M. Sixt, R. Wedlich-Soldner, Lifeact mice for studying F-actin dynamics. *Nat Methods* **7**, 168-9 (2010).

31. P. Mombaerts, J. Iacomini, R. S. Johnson, K. Herrup, S. Tonegawa, V. E. Papaioannou, RAG-1-deficient mice have no mature B and T lymphocytes. *Cell* **68**, 869-877 (1992).

32. M. Hons, A. Kopf, R. Hauschild, A. Leithner, F. Gaertner, J. Abe, J. Renkawitz, J. V. Stein, M. Sixt, Chemokines and integrins independently tune actin flow and substrate friction during intranodal migration of T cells. *Nat Immunol* **19**, 606-616 (2018).

33. A. D. Edelstein, M. A. Tsuchida, N. Amodaj, H. Pinkard, R. D. Vale, N. Stuurman, Advanced methods of microscope control using muManager software. *J Biol Methods* **1**, e10 (2014).

34. J. Y. Tinevez, N. Perry, J. Schindelin, G. M. Hoopes, G. D. Reynolds, E. Laplantine, S. Y. Bednarek, S. L. Shorte, K. W. Eliceiri, TrackMate: An open and extensible platform for single-particle tracking. *Methods* **115**, 80-90 (2017).

35. E. van Grinsven, J. Textor, L. S. P. Hustin, K. Wolf, L. Koenderman, N. Vrisekoop, Immature Neutrophils Released in Acute Inflammation Exhibit Efficient Migration despite Incomplete Segmentation of the Nucleus. *J Immunol* **202**, 207-217 (2019).

36. W. S. Pear, J. P. Miller, L. Xu, J. C. Pui, B. Soffer, R. C. Quackenbush, A. M. Pendergast, R. Bronson, J. C. Aster, M. L. Scott, D. Baltimore, Efficient and rapid induction of a chronic myelogenous leukemia-like myeloproliferative disease in mice receiving P210 bcr/abl-transduced bone marrow. *Blood* **92**, 3780-92 (1998).

37. S. Morita, T. Kojima, T. Kitamura, Plat-E: an efficient and stable system for transient packaging of retroviruses. *Gene Ther* **7**, 1063-6 (2000).

38. E. Schweighoffer, L. Vanes, J. Nys, D. Cantrell, S. McCleary, N. Smithers, V. L. Tybulewicz, The BAFF Receptor Transduces Survival Signals by Co-opting the B Cell Receptor Signaling Pathway. *Immunity* **38**, 475-88 (2013).

39. J. V. Abella, C. Galloni, J. Pernier, D. J. Barry, S. Kjaer, M. F. Carlier, M. Way, Isoform diversity in the Arp2/3 complex determines actin filament dynamics. *Nat Cell Biol* **18**, 76-86 (2016).

40. A. G. Clark, K. Dierkes, E. K. Paluch, Monitoring actin cortex thickness in live cells. *Biophys J* **105**, 570-80 (2013).

41. Y. Benjamini, Y. Hochberg, Controlling the False Discovery Rate: A Practical and Powerful Approach to Multiple Testing. *Journal of the Royal Statistical Society: Series B (Methodological)* **57**, 289-300 (1995).

42. Y. Benjamini, A. M. Krieger, D. Yekutieli, Adaptive linear step-up procedures that control the false discovery rate. *Biometrika* **93**, 491-507 (2006).

Acknowledgments:

We thank Erik Sahai and Michael Way for critical reading of this manuscript. We thank the Advanced Light Microscopy, Flow Cytometry and Biological Research Facilities of the Francis Crick Institute for microscopy, flow cytometry and for animal husbandry. We thank Chou-Long Huang, Dario Alessi and Sung-Sen Yang for mouse strains. We thank Rachel Toth for generation of plasmids, and the MRC Protein Phosphorylation Unit for antibodies.

Funding:

VLJT was supported by the Francis Crick Institute which receives its core funding from Cancer Research UK (FC001194), the UK Medical Research Council (FC001194), and the Wellcome Trust (FC001194). LLdB was funded by an Imperial College London President's PhD Scholarship. For the purpose of Open Access, the author has applied a CC-BY public copyright licence to any Author Accepted Manuscript version arising from this submission.

Author Contributions:

Conceptualization: LLdB, VLJT

Data curation: LLdB

Formal analysis: LLdB, SM

Funding acquisition: VLJT, LLdB

Investigation: LLdB, SM, LV, DH, JBOM

Methodology: LLdB, RK

Project administration: VLJT

Resources: JBOM, RK, DH, LV

Supervision: VLJT, LLdB

Visualization: LLdB

Writing – original draft: LLdB, VLJT

Writing – review & editing: LLdB, VLJT

Competing interests:

The authors have no competing interests.

Data and materials availability:

Mouse strains available on request.

List of Supplementary Materials:

Materials and Methods

Figures S1 to S3

Videos S1 to S6

References 27-42

Figure 1

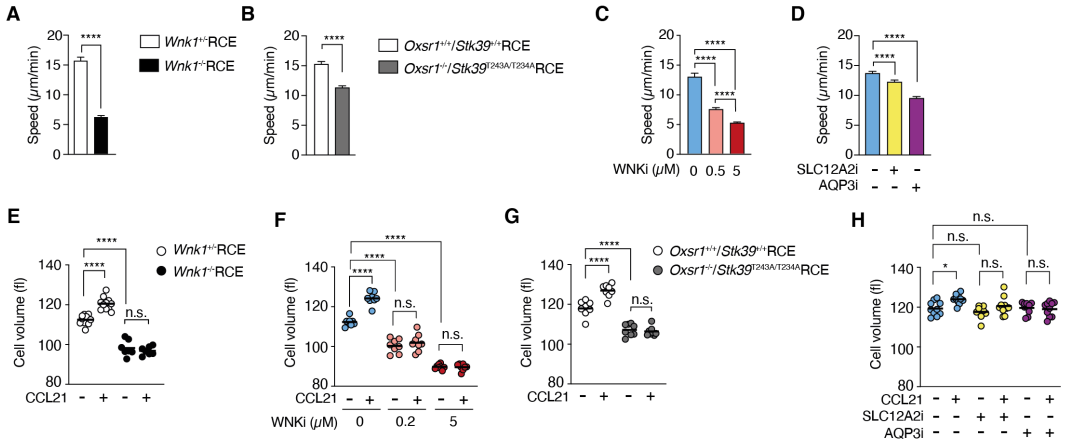

Figure 1. WNK1 pathway proteins are required for CCL21-induced migration and volume changes of CD4$^+$ T cells.

(**A-D**) Mean (±95% CI) speed of mouse naive CD4$^+$ T cells of the indicated genotypes or treated with inhibitors migrating on ICAM-1 under agarose in response to CCL21. (**E-H**) Cell volume of naïve CD4$^+$ T cells of the indicated genotypes, or treated with inhibitors, stimulated with CCL21 for 20 min where indicated. Dots represent modal cell volume from 1 mouse, lines show means. Data from ≥532 (A-D) cells and ≥6 (E), 8 (F-G), and 10 (H) mice. Data pooled from at least 2 (A-D) or 3 (E-H) independent experiments. Statistical analysis was carried using Mann-Whitney (A-B) to generate *p*-values, and Kruksal-Wallis (C-D) or 1-way ANOVA (E-H) to generate FDR-adjusted *q*-values; n.s., not significant, *0.01 < q < 0.05, ****p or q < 0.0001.

Figure 2

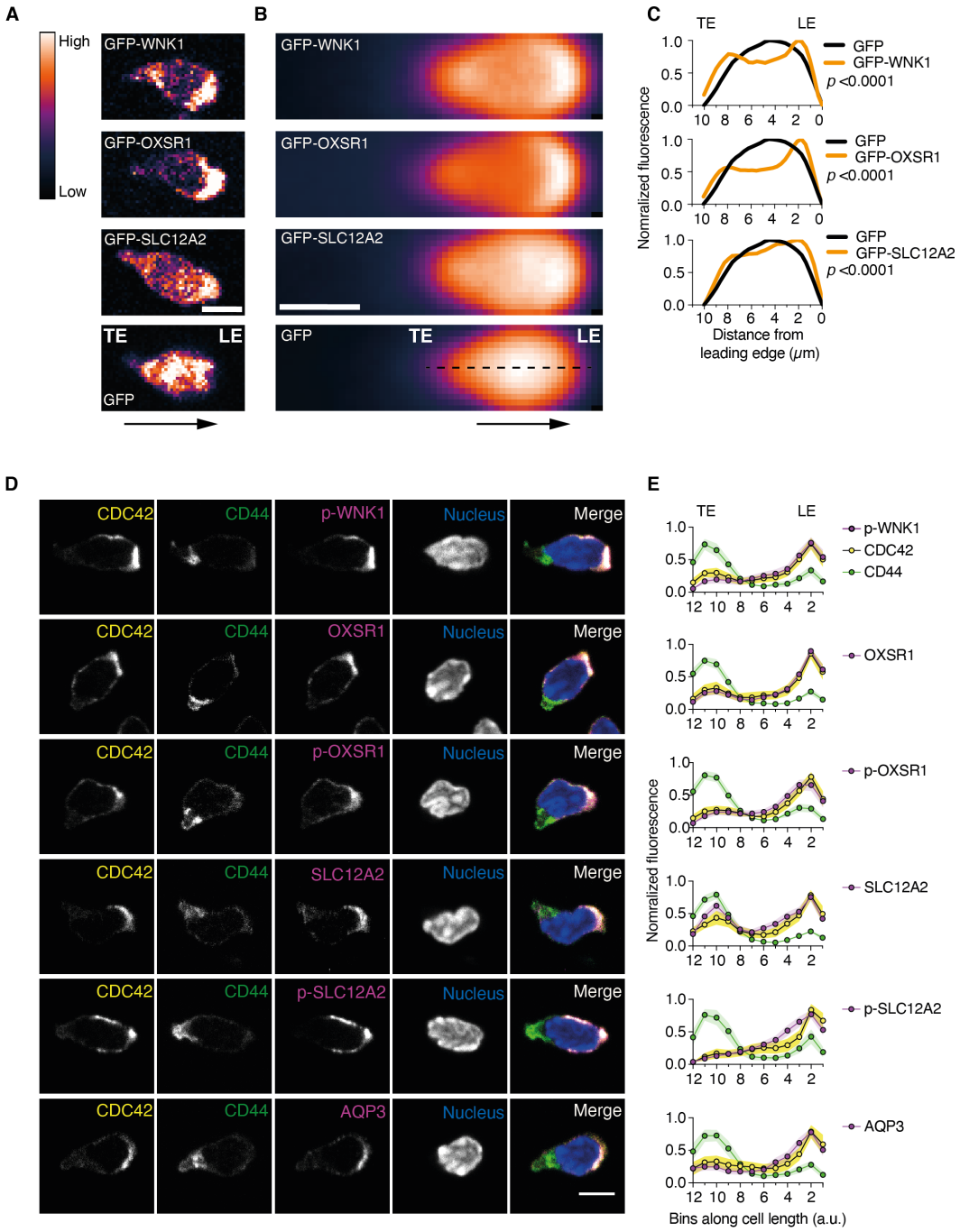

Figure 2. WNK1 pathway proteins polarize to the leading edge of migrating CD4$^+$ T cells.

(**A-C**) Naïve CD4$^+$ T cells expressing GFP-tagged WNK1 pathway proteins or GFP alone were imaged migrating on ICAM-1 under agarose in response to CCL21; example images are shown (A). Arrow indicates direction of migration. Individual cell images were aligned in the direction of migration to visualize GFP distribution (B).

Intensity projection of GFP-tagged proteins along the dashed line in B compared to EV-GFP (C). Lines represent mean (±95% CI). *p*-values for difference in distribution of GFP-tagged WNK1, OXSR1 and SLC12A2 compared to GFP alone were determined using a 2-way ANOVA. (**D-E**) Naïve $CD4^+$ T cells migrating in response to CCL21 on ICAM-1 were fixed and stained with antibodies against the indicated (phospho-) proteins. Typical example images of 6 cells showing staining for individual proteins and a merged image (D). Mean (±95% CI) normalized intensity projections of WNK1 pathway proteins in relation to the LE and TE, as indicated by highest levels of CDC42 and CD44 respectively (E). Cell lengths were binned into 12 bins per cell. Scale bars, 5 μm. $n \geq 1244$ cells/projection from 1 experiment, representative of at least 2 experiments (B, C). ≥ 47 cells pooled from at least 2 experiments per protein (E). TE, trailing edge; LE, leading edge; a.u., arbitrary units.

Figure 3

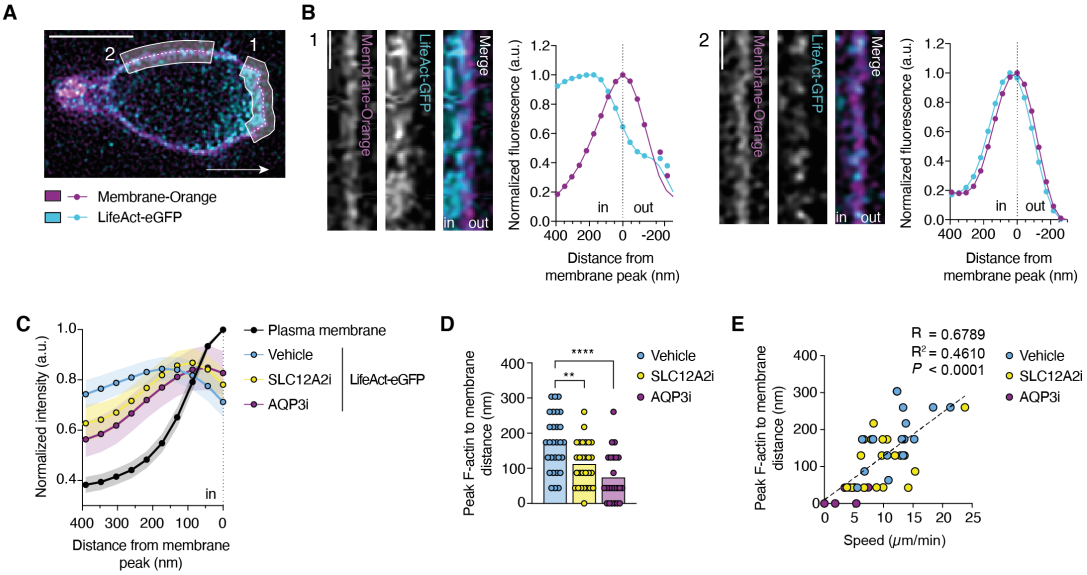

Figure 3. The WNK1 pathway regulates spacing between the plasma membrane and the F-actin cytoskeleton.

(**A-E**) Instant structured illumination microscopy of LifeAct-eGFP expressing naïve CD4$^+$ T cells stained with CellMask Orange to show plasma membrane (PM), migrating on ICAM-1 coated dishes under CCL21-containing agarose. Representative image of a migrating cell indicating a region of the leading edge (1) and the side of the cell (2); white arrow shows direction of migration; scale bar, 5 μm. (A). Fluorescence images of linearized regions 1 and 2 from A and graphs showing normalized LifeAct-eGFP and PM fluorescence as a function of distance from peak PM fluorescence, indicated by the dotted line; scale bar, 1 μm (B). Mean (±95% CI) LifeAct-eGFP and PM fluorescence as a function of distance from peak PM fluorescence (dotted line) in CD4$^+$ T cells treated with inhibitors or vehicle (C). Distance of peak LifeAct-eGFP fluorescence to the PM; each dot represents a single frame from one cell, columns represent mean (D). Distance of peak LifeAct-eGFP fluorescence to the PM as a function of migration speed in CD4$^+$ T cells treated with inhibitors or vehicle; dashed line, linear regression; R, correlation coefficient (E). a.u., arbitrary units. ≥23 (C, D) and 42 (E) cells. Data are pooled from at least 3 experiments. One-way ANOVA (D) or Pearson's correlation test (E), **$0.001 < q < 0.01$, ****$q < 0.0001$.

Figure 4

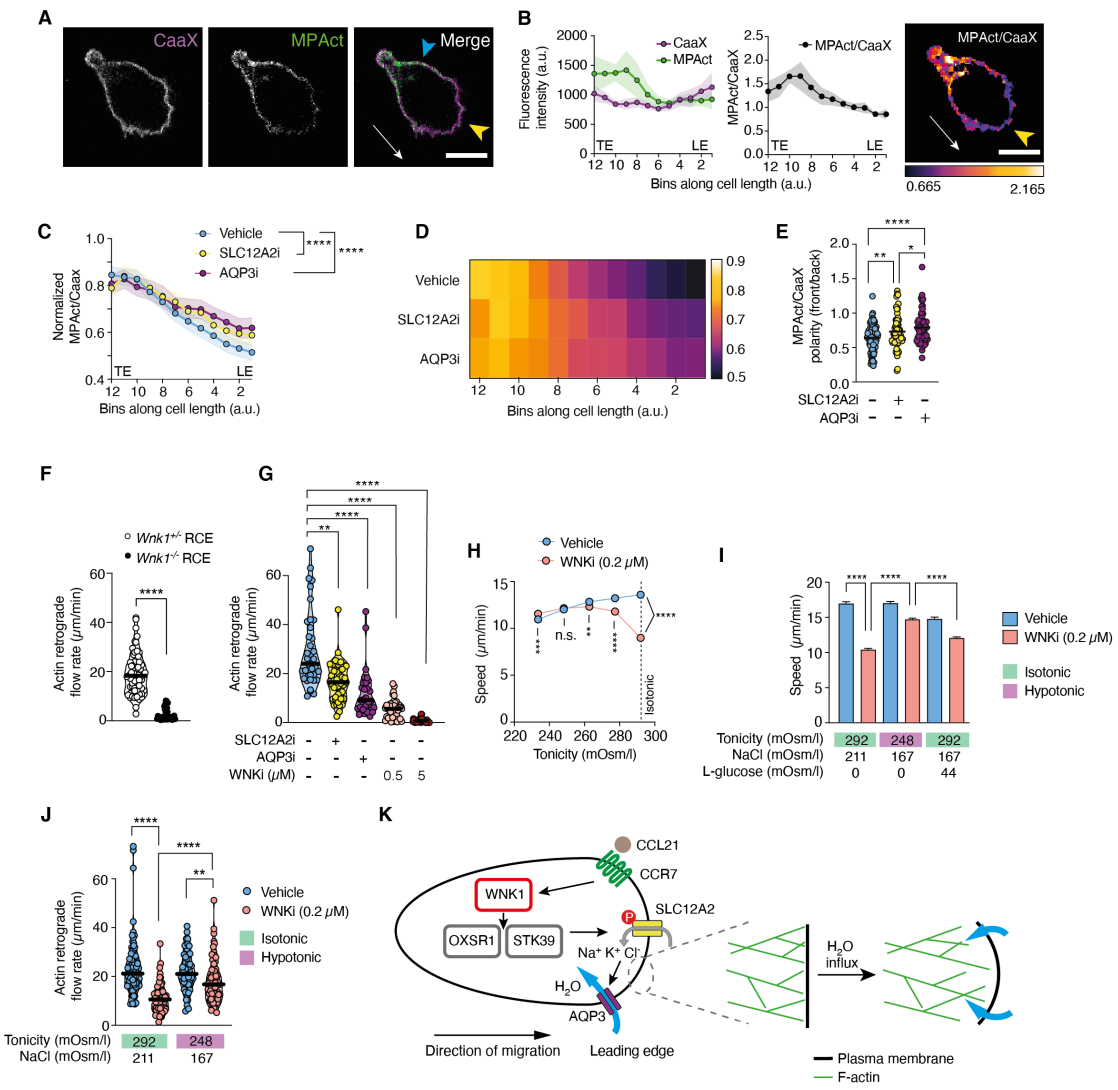

Figure 4. WNK1-regulated water influx regulates actin polymerization rate in migrating CD4⁺ T cells.

(**A-E**) Naïve CD4⁺ T cells co-expressing GFP-CaaX (CaaX) and MPAct-mCherry (MPAct), were imaged migrating in response to CCL21 on ICAM-1 under agarose. Representative images of CaaX and MPAct fluorescence in a cell showing direction of migration (white arrow), LE (yellow arrowhead) and side of cell (blue arrowhead) (A). Mean (±95% CI) CaaX and MPAct fluorescence and MPAct/CaaX ratio in the same cell as shown in A, averaged over 20 frames taken every 15 s; image shows MPAct/CAAX ratio of the cell in A (B). Mean (±95% CI) normalized MPAct/CaaX ratios along full cell length and width taken from multiple cells treated inhibitor or vehicle (C).

Heatmap of MPAct/CaaX ratio along the length of the cell (D). MPAct/CaaX polarity ratio, where the mean of the front 3 bins was divided by the mean of the back 3 bins using the same data as in C-D; each dot shows data from one cell, line shows mean (E). (**F-G, J**) Naïve $CD4^+$ T cells expressing LifeAct-eGFP of the indicated genotypes or treated with inhibitor or vehicle, were stimulated with CCL21 under agarose on a PEG-coated dish and imaged using TIRFM. Dots represent F-actin flow rates within single cells, lines represent median. (**H-I**) Mean (±95% CI) speed of $CD4^+$ T cells migrating on ICAM-1 under agarose in response to CCL21 in the presence or absence of WNKi. Tonicity of agarose was varied as indicated. (**K**) Proposed model: CCL21 binding to CCR7 at the leading edge of the migrating $CD4^+$ T cell results in activation of WNK1, which phosphorylates and activates OXSR1 and STK39. These in turn phosphorylate SLC12A-family proteins, resulting in entry of Na^+, K^+ and Cl- ions into the cell and consequent water entry through AQP3 by osmosis. Water entry swells the PM, creating space into which actin filaments can extend, thereby protruding the cell forward. LE, leading edge; TE, trailing edge; a.u., arbitrary units. Scale bars, 5 µm. ≥61 (C-E), ≥31 (F-G), ≥ 1769 (H), ≥ 5795 (I) and > 55 (J) cells per condition. Data are pooled from at least 2 (C-G), 3 (J) or 4 (H-I) experiments. 2-way ANOVA (C), 1-way ANOVA (E, H, I), Mann-Whitney (F) or Kruskal-Wallis (G, J); *$0.01 < q < 0.05$, **$0.001 < q < 0.01$, **** p or $q < 0.0001$.

SUPPLEMENTARY MATERIAL

MATERIALS AND METHODS

Mice

Mice with a conditional allele of *Wnk1* containing loxP sites flanking exon 2 (*Wnk1*^{tm1Clhu},*Wnk1*^{fl}) (*27*), with a deletion of exon 2 of *Wnk1* (*Wnk1*$^{tm1.1Clhu}$, *Wnk1*$^{-}$) (*4*), with a conditional allele of *Oxsr1* containing loxP sites flanking exons 9 and 10 (*Oxsr1*$^{tm1.1Ssy}$, *Oxsr1*^{fl}) (*28*), with a tamoxifen-inducible Cre in the ROSA26 locus (*Gt(ROSA)26Sor*$^{tm1(Cre/ESR1)Thl}$, *ROSA26*^{CreERT2}, RCE) (*29*), with an allele of *Stk39* encoding STK39-T243A (*Stk39*$^{tm1.1Arte}$, *Stk39*^{T243A}) (*5*) that cannot be activated by WNK1, expressing LifeAct-eGFP (Tg(CAG-EGFP)#Rows) (*30*) or deficient for RAG1 (*Rag1*^{tm1Mom}, *Rag1*$^{-}$) (*31*) have been described before. C57BL/6J mice were provided by the Biological Research Facility of the Francis Crick Institute. All mice were maintained on a C57BL/6J background and intercrossed as required to generate strains with multiple genetically altered alleles. Animals were housed in independently ventilated cages under specific pathogen-free conditions and given food and water *ad libitum*. All mice were age- and sex-matched within an experiment. All experiments were approved by the Francis Crick Institute Animal Welfare Ethical Review Board and were carried out under the authority of a Project Licence granted by the UK Home Office.

Bone marrow chimeras

Bone marrow cells from *Wnk1*$^{fl/+}$RCE and *Wnk1*$^{fl/-}$RCE mice or from LifeAct-eGFP*Wnk1*$^{fl/+}$RCE and LifeAct-eGFP*Wnk1*$^{fl/-}$RCE mice or from *Oxsr1*$^{+/+}$*Stk39*$^{+/+}$RCE, *Oxsr1*$^{fl/fl}$*Stk39*$^{+/+}$RCE, and *Oxsr1*$^{fl/fl}$/*Stk39*$^{T234A/T234A}$RCE mice were transferred intravenously into irradiated (5 Gy, ^{37}Cs source) RAG1-deficient recipient mice which were maintained on 0.02% enrofloxacin (Baytril, Bayer Healthcare) for 4 weeks. In all cases the sex of the donor and recipient mice was matched. The hematopoietic

compartment was allowed to reconstitute for at least 8 weeks after bone marrow transfer. In all experiments, control and experimental chimeric mice or cells derived from them were always sex-matched.

In vivo deletion of floxed alleles

Tamoxifen treatment of *Wnk1*$^{fl/+}$RCE and *Wnk1*$^{fl/-}$RCE bone marrow chimeras was used to generate *Wnk1*$^{+/-}$RCE and *Wnk1*$^{-/-}$RCE T cells. Tamoxifen treatment of *Oxsr1*$^{+/+}$*Stk39*$^{+/+}$RCE, *Oxsr1*$^{fl/fl}$*Stk39*$^{+/+}$RCE, and *Oxsr1*$^{fl/fl}$/*Stk39*$^{T234A/T234A}$RCE bone marrow chimeras was used to generate *Oxsr1*$^{+/+}$*Stk39*$^{+/+}$RCE, *Oxsr1*$^{-/-}$*Stk39*$^{+/+}$RCE, and *Oxsr1*$^{-/-}$/*Stk39*$^{T234A/T234A}$RCE T cells. Mice were injected intraperitoneally with 2 mg tamoxifen in corn oil (Sigma-Aldrich) on 3 (*Wnk1*^{fl}) or 5 (*Oxsr1*^{fl}) consecutive days. Mice were sacrificed 7 (*Wnk1*^{fl}) or 21 (*Oxsr1*^{fl}) days after initial tamoxifen injection to harvest T cells.

T cell purification and culture

To isolate naïve CD4^{+} T cells, mouse lymph node cells were incubated with biotin-conjugated antibodies to CD44 (IM7) and CD25 (PC61.5) (both from ThermoFisher), CD11c (N418), Ly6G (RB6-8C5), CD8α (53-6.7), B220 (RA3-6B2) and TER119 (TER-119) (all from BioLegend) and CD19 (1D3, BD Biosciences), and antibody-bound cells were removed with streptavidin-coated Dynabeads (ThermoFisher) using magnetic-activated cell sorting according to the manufacturer's instructions. Isolated T cells were rested overnight at 37°C and 5% CO_2 at 1x10^{6} cells/ml in R10 medium, which consisted of RPMI 1640 (Sigma) supplemented with 10% fetal calf serum (FCS), 100 U/ml penicillin, 100 µg/ml streptomycin, 2 mM L-glutamine, 1 mM sodium pyruvate, non-essential amino acids, 100 µM 2-mercaptoethanol (all Sigma-Aldrich) and 20 mM HEPES (Gibco).

T cell migration under agarose

8-well polymer or glass chamber μ-slides (ibidi, 80821 or 80827) were coated with recombinant mouse ICAM-1-Human-Fc chimera (RnD, 796-IC) at 3 μg/ml in PBS overnight at 4°C. Slides were washed 3x with PBS, blocked with 2% bovine serum albumin (BSA) (Sigma-Aldrich), and washed 3x again. Agarose gel preparation was adapted from a previously described method (*32*). Agarose (0.5%, UltraPure Agarose, ThermoFisher) in R10-equivalent medium was prepared at 50°C, and, if required, mouse CCL21 (250 ng/mL RnD, 457-6C) and inhibitors [WNK463, (WNKi, MedChemExpress), bumetanide (SLC12Ai, 20 μM, Abcam) or DFP00173 (AQP3i, 20 μM, Axon Med Chem)] or equivalent amounts of vehicle control (DMSO, ThermoFisher) were added, and the mixture immediately plated onto the μ-slides. The agarose was cooled at 4°C for 1 h, and then equilibrated at 37°C and 5% CO_2 for at least 30 min. To change the osmolarity of the gel, part of the solution was replaced with NaCl-free HBSS to generate a gel of the required osmolarity. For isotonic agarose gels with reduced NaCl, the NaCl-free HBSS was supplemented with L-glucose (Sigma). Osmolarity was verified using an osmometer (Model 3250, Advanced Instruments).

T cells stained with CellTrace Violet (CTV, 1 μM, ThermoFisher) were resuspended in a small volume of R10 medium containing propidium iodide (1.5 μM) and injected under the agarose gel with a pipette. Cells were acclimatized at the microscope for at least 30 min in a humidified chamber at 37°C and 5% CO_2 and then imaged every 15 s for 10 min using a Nikon Ti2 Eclipse microscope with an LED illumination system. Images were acquired with a Nikon 20x (0.75 NA) Ph2 plan apo objective, at 2048x2048 resolution in 16-bit using Micro-Manager (*33*). Cells were tracked using the FIJI plugin TrackMate (*34*). Propidium iodide-containing dead cells, and tracks shorter than half the video length were excluded. To determine cell shapes, binary images were produced from the CTV signal from one still frame per video stack using the FIJI ‘triangle’ auto-thresholding algorithm. Cell profiles were smoothed using the ‘open’

binary function and particles between 38 and 60 μm^2 were detected with the 'analyze particle' tool.

T cell migration in a Collagen-I matrix

To study T cell migration in a collagen-I matrix a previously described method was adapted (*35*). CTV-labeled $CD4^+$ T cells (2 x 10^6 cells/ml) in R10 medium containing rat tail Collagen-I (1.5 mg/ml, Ibidi) and CCL21 (250 ng/ml) were mixed on ice and plated into wells of a 15-well angiogenesis µ-slide (Ibidi) and incubated at 37°C and 5% CO_2 for 30 min to allow the collagen to polymerize. R10 medium containing CCL21, propidium iodide (1.5 µM) and inhibitors or vehicle control if required, was added to the wells and slides incubated in a humidified chamber on the microscope at 37°C and 5% CO_2 for a further 30 min. Cells were imaged using a Zeiss LSM880 with an AiryScan detector, a 405 nm laser to excite both CTV and propidium iodide and a Zeiss 10x plan apo (0.45 N.A.) air objective. A z-stack consisting of 14 z-slices with an 8 µm spacing were acquired every 15 s for 5 - 10 min. Cells were tracked using the FIJI plugin TrackMate. Propidium iodide-positive cells and cells that were tracked for less than 1/3 of the video length were excluded from the analysis.

Generation of $CD4^+$ T cells expressing GFP-WNK1, GFP-OXSR1 and GFP-SLC12A2

DNA fragments encoding open reading frames for GFP-WNK1, GFP-OXSR1 and GFP-SLC12A2 were inserted into the MIGR1 retroviral vector (*36*), replacing the IRES-GFP sequence, such that fusion proteins were expressed from the 5' LTR of the vector. In all cases the eGFP was fused in-frame to the N-terminus of the human WNK pathway proteins. The GFP-WNK1 and GFP-SLC12A2 constructs were generated by the MRC Protein Phosphorylation Unit. All constructs were validated by DNA sequencing.

Plasmid DNA for MIGR1 vectors expressing GFP-WNK1, GFP-OXSR1 or GFP-SLC12A2 and MIGR1 expressing GFP only were transfected into PlatE cells (*37*) to generate medium containing infectious retrovirus. This was used to infect bone marrow cells from C57BL/6J mice that were in turn used to reconstitute irradiated (5 Gy, ^{37}Cs source) RAG1-deficient mice as previously described (*38*).

Live cell imaging of T cells expressing WNK1 pathway proteins

$CD4^+$ T cells expressing GFP-tagged WNK1 pathway proteins were purified from lymph nodes of bone marrow chimeras by flow cytometric sorting for GFP^+ T cells. Sorted cells were incubated overnight in R10 medium at 37°C and 5% CO_2 and then injected under agarose in an 8-well plastic bottom µ-slide containing CCL21 as described earlier. Cells were placed in a humidified chamber at 37°C and 5% CO_2 on a Zeiss LSM 880 inverted microscope for 30 min, and then imaged by confocal microscopy with a 63x plan apo (1.4 N.A.) oil-immersion objective. Cells were imaged every 15 s for 5 min in a single z-plane proximal to the coverslip. To determine the localization of GFP or GFP-tagged proteins in migrating T cells we used the FIJI plugin VirusTracker (*39*). The plugin detects the direction of migration and was set to capture a 20 µm-long region of interest along the length of the cell. Images of these cell shapes were projected on top of each other using the mean intensity projection option.

Imaging of WNK1 pathway proteins in fixed T cells

15-well angiogenesis or 18- well µ-slides (ibidi, 81506 or 81816) were coated with 3 µg/ml mouse ICAM-1-human Fc fusion protein overnight at 4°C. Slides were washed 3x with PBS, blocked with 2% BSA in PBS for 20 min at room temperature, and washed again three times. Naïve $CD4^+$ T cells that had been incubated overnight at 37°C were resuspended in RPMI containing 0.5% BSA, added to the µ-slides, and allowed to adhere for 1 h at 37°C. Cells were stimulated with 250 ng/ml CCL21 for 20 min, and then fixed in 4% paraformaldehyde for 15 min at room temperature. Cells were washed

with PBS, blocked in 1% BSA in PBS (blocking buffer) for 20 min, permeabilized with 0.1% Tween20 in PBS for 15 min, washed with PBS and stained in blocking buffer overnight at 4°C with anti-CDC42 (B-8 mouse monoclonal, Santa Cruz), biotin-conjugated anti-CD44 (IM7 rat monoclonal, BioLegend) and one of these primary antibodies: anti-p-WNK1 (S382), anti-OXSR1, anti-p-OXSR1 (S325), anti-SLC12A2, anti-p-SLC12A2 (T203/T207/T212) (all sheep polyclonal sera from MRC Protein Phosphorylation Unit) or anti-AQP3 (NBP1-97927 rabbit polyclonal, Novus Biologicals). Cells were washed with PBS and incubated in blocking buffer for 1 h with Streptavidin-AlexaFluor 488 (S11223, Molecular Probes), goat anti-Mouse IgG-AlexaFluor 555 (A-21424), and either goat anti-rabbit IgG-AlexaFluor 647 (A-21245) or donkey anti-sheep IgG-AlexaFluor 647 (A-21448, all from ThermoFisher). Cells were washed twice with 0.1% Tween20 in PBS and once with PBS containing DAPI to visualize the nucleus. Cells were washed once and covered with VectaMount AQ aqueous mounting medium (Vector Laboratories) and stored at 4°C until imaging.

Cells were imaged on a Leica SP8 FALCON inverted confocal microscope with a 63x plan apo (1.4 NA) oil-immersion objective. Fluorophores were excited with a white light laser. Cells were imaged in z-stacks consisting of 7-9 z-slices with a 1 µm spacing. To determine localization of WNK1 pathway proteins, CDC42 and CD44 were used to determine the leading and trailing edges (LE and TE) respectively. A line the full width of the cell was drawn along the length of the cell from the LE to the TE. Average fluorescence intensities were determined for each of 12 bins along the cell length. Intensity profiles were normalized from 0-1, where 0 was the lowest signal and 1 the highest signal per protein, per cell. Binned normalized fluorescence intensities were used to calculate the correlations between LE and TE markers and WNK1 pathway proteins.

Cell volume measurement

T cells were rested overnight in R10 medium. If required, WNK463 or vehicle control was added for 20 min and then CCL21 for a further 20 min. Cells were resuspended in CASYton fluid (Cambridge Bioscience) and median cell volumes measured on a CASY cell counter (Cambridge Bioscience).

Flow cytometric analysis of F-actin

Overnight-rested mouse naïve $CD4^+$ T cells were placed in RPMI, 0.5% BSA and stimulated with CCL21 for the required time. Cells were immediately fixed in 4% paraformaldehyde for 15 min. Cells were washed with PBS, permeabilized with 0.1% Tween20 in PBS for 15 min, and blocked for 1 h in 2% BSA in PBS. Cells were stained with phalloidin conjugated to iFluor-488 (Abcam) in blocking buffer for 1 h at room temperature, washed twice with 0.1% Tween20, and once with PBS. Cells were analyzed on an LSRII flow cytometer (BD Biosciences) and mean fluorescence intensity was quantified using FlowJo (BD Biosciences).

TIRF microscopy of F-actin retrograde flow

35 mm round glass-bottom dishes (Greiner Bio-One) were cleaned with 1 M HCl for 15 min and washed three times with water. Dishes were plasma-activated for 30 s (HPT-100, Henniker Plasma) and coated with 0.2 mg/ml poly(L-lysine)-graft-PEG (SuSoS) in PBS overnight at 4°C, blocked with 2% BSA in PBS for 20 min, and washed three times with PBS. Overnight-rested mouse naïve $CD4^+$ T cells constitutively expressing LifeAct-eGFP were injected under agarose containing CCL21 and either inhibitors or vehicle control. Cells were imaged at 37°C and 5% CO_2 using an Olympus IX83 total internal reflection fluorescence (TIRF) microscope with a 150x 1.45 NA TIRF apo oil-immersion objective every 1 s for 1 min. Actin flow rates were determined from kymographs generated using FIJI.

Analysis of membrane proximal F-actin

Mouse naïve $CD4^+$ T cells were transfected with C1-MPAct-mCherry (Addgene #155222, gift from Tobias Meyer) and C1-eGFP-CaaX (Addgene #86056, gift from Lei Lu) plasmids using the X-001 program on a Nucleofector (Lonza) and rested overnight in T cell medium (Lonza). $GFP^+mCherry^+$ T cells were sorted and incubated in R10 medium for at least 2 h at 37°C and 5% CO_2. Cells were injected under agarose containing CCL21 and inhibitors or vehicle control and allowed to acclimatize for at least 30 min in a humidified chamber on the microscope at 37°C and 5% CO_2. Cells were imaged using a Leica SP8 FALCON confocal inverted microscope, equipped with a 63x plan apo (1.4 NA) oil-immersion objective every 15 s for 2.5 or 5 min. Cells were excited using a white light source at 488 nm for eGFP-CaaX and at 585 nm for MPAct-mCherry, and acquired simultaneously.

To analyze the distribution of the MPAct probe, one random frame per migrating cell was selected using FIJI. Bias was avoided by selecting frames using only the GFP-CaaX signal. The leading edge of the cell was determined from the direction of migration. A line the full length and width of the cell was draw from the front to the back of the cell. Average fluorescence intensities were determined for each of 12 bins along the cell length. Fluorescence intensity levels were normalized with the highest intensity value per fluorophore, per cell set to 1. The normalized MPAct-mCherry signal was divided by the normalized eGFP-CaaX signal to generate the MPAct/CaaX ratio. Polarization of the MPAct signal was determined by dividing the MPAct/CaaX ratio in the front 3 bins by the ratio in the rear 3 bins.

Analysis of plasma membrane to F-actin spacing

Overnight-rested mouse naïve $CD4^+$ T cells constitutively expressing LifeAct-eGFP were labeled with CellMask Orange (ThermoFisher) to stain the plasma membrane following the manufacturer's instructions. Cells were washed once with PBS, resuspended in R10 medium and injected under CCL21- and inhibitor-containing

agarose in a glass bottom 8-well μ-slide dishes (Ibidi) pre-coated with ICAM-1. Cells were imaged by instant structured illumination microscopy (iSIM) using an iSIM microscope (VisiTech) with an Olympus 150x TIRF apo (1.45 NA) oil-immersion objective. Cells were simultaneously excited at 488 nm for LifeAct-eGFP and 561 nm for CellMask Orange. Emission fluorescence was split with a dichroic mirror with a long-pass filter at 561 nm and was simultaneously detected using 2 sCMOS cameras (Prime BSI Express, Teledyne Photometrics). Cells were imaged every 250 ms for a total of 30 s in a single z-plane proximal to the coverslip. To correct for chromatic aberration and camera alignment, 0.5 μm TetraSpeck fluorescent beads (ThermoFisher) were imaged after each session using the same acquisition settings as the cells.

Images were deconvoluted using Huygens software (Scientific Volume Imaging) with the 'Normal' deconvolution template. A random frame from the time-lapse series was chosen while viewing only the plasma membrane stain to avoid bias. The leading edge of the cell was determined from the direction of migration. Adapting a previously described analysis protocol (*40*), a 30-pixel wide line was drawn along the leading edge, with the plasma membrane placed in the middle of the line. The line and the data within it were straightened out and 20-pixel wide overlapping lines were drawn perpendicular to the plasma membrane signal, along the length of the leading edge. Fluorescence intensity data were normalized from 0-1, and the intensity profiles in each 20-pixel wide line were manually aligned according to the peak of plasma membrane fluorescence intensity. The distance between the peak plasma membrane signal and the peak F-actin signal was calculated within each line, with the peak of F-actin defined as the highest LifeAct-eGFP fluorescence intensity within 400 nm of the plasma membrane.

Statistical analysis

To determine statistical significance between two unpaired groups, we used a Mann-Whitney U test. To determine statistical significance when there were more than two groups and one variable, we used either a Kruskal-Wallis test when the data was not normally distributed, and unpaired and unmatched, or a 1-way ANOVA when the data was normally distributed and unmatched. When comparing multiple paired groups, we used a Friedman test. When comparing two or more groups, but with two variables (i.e. time and inhibitor/genotype) a 2-way ANOVA or a mixed effects analysis was used. To correct *p*-values for multiple comparisons we used the False Discovery Rate (FDR) method with the two-stage step-up to generate *q*-values (*41, 42*). $q < 0.05$ was used as a cut-off to determine statistical significance. In cases where there was no multiple comparison correction (Mann-Whitney tests), $p < 0.05$ was used as a cut-off to determine statistical significance. All statistical analysis was performed using Prism (GraphPad).

Supplementary Figures

Figure S1

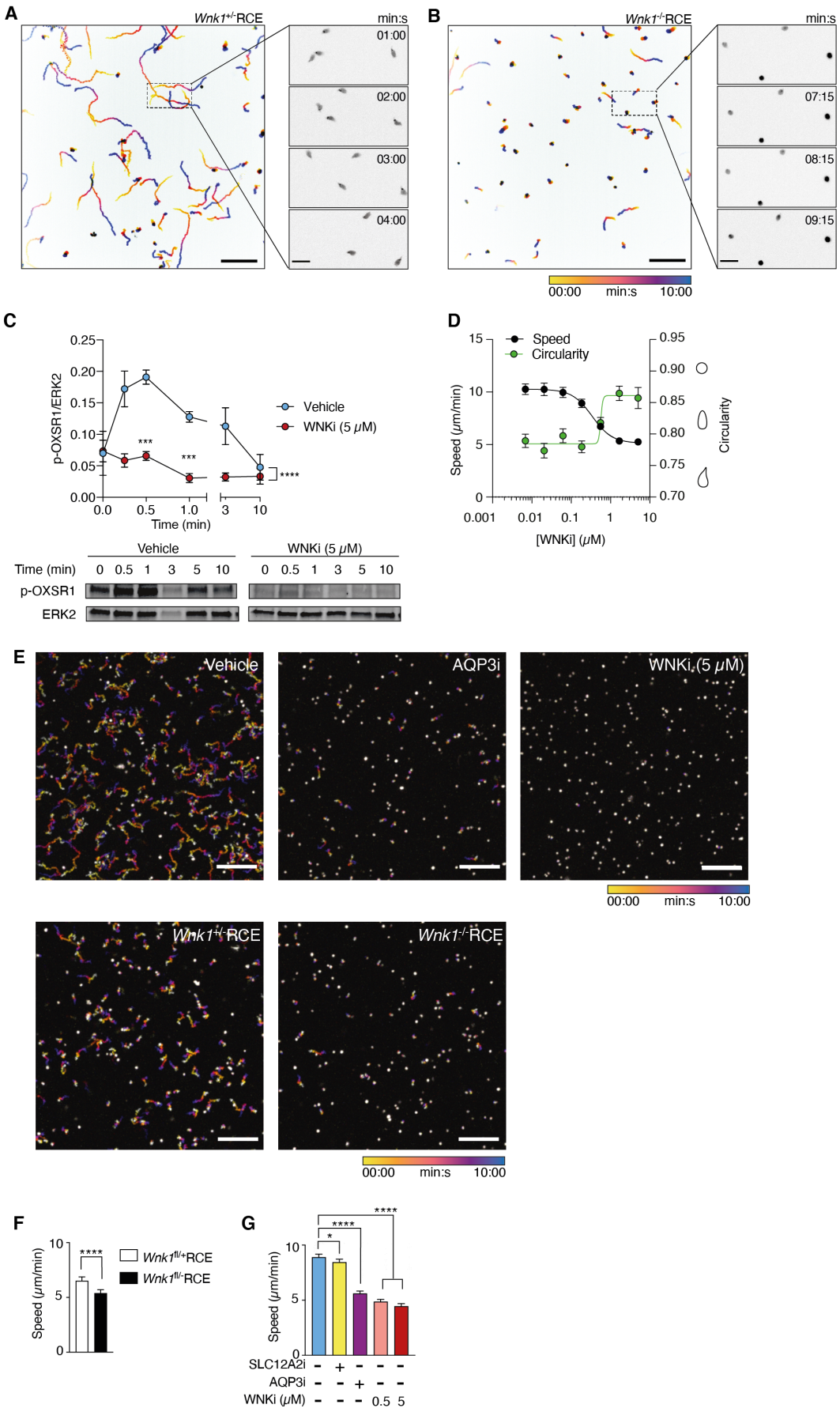
A
Wnk1+/-RCE
min:s
01:00
02:00
03:00
04:00
B
Wnk1-/-RCE
min:s
07:15
08:15
09:15
00:00
min:s
10:00
C
p-OXSR1/ERK2
Time (min)
Vehicle
WNKi (5 μM)
***
****
Time (min)
0 0.5 1 3 5 10
0 0.5 1 3 5 10
p-OXSR1
ERK2
D
Speed
Circularity
Speed (μm/min)
Circularity
[WNKi] (μM)
E
Vehicle
AQP3i
WNKi (5 μM)
Wnk1+/-RCE
Wnk1-/-RCE
00:00
min:s
10:00
F
Speed (μm/min)
Wnk1fl/+RCE
Wnk1fl/-RCE
****
G
Speed (μm/min)
SLC12A2i
AQP3i
WNKi (μM)
0.5 5

Figure S1. WNK1 pathway proteins are required for CCL21-induced migration of CD4$^+$ T cells in confinement.

(**A-B**) Time-projected example images of CTV-labelled mouse naïve CD4$^+$ T cells of the indicated genotypes migrating on ICAM-1 under agarose in response to CCL21. Scale bar: 100 µm, zoomed section scale bar: 20 µm. (**C**) Mean (±SEM) levels of phosphorylated OXSR1 (p-OXSR1), normalized to the levels of ERK2, in mouse naïve CD4$^+$ T cells stimulated with CCL21 for the indicated times, determined by immunoblotting total cell lysates with antibodies to p-OXSR1 and ERK2. Example immunoblots shown below graph. (**D**) Mean (±95% CI) speed and circularity (example shapes on y-axis) of mouse naive CD4$^+$ T cells treated with inhibitors or vehicle alone, migrating on ICAM-1 under agarose in response to CCL21. (**E**) Z- and time-projected example images of CTV-labelled mouse naïve CD4$^+$ T cells of the indicated genotypes, or treated with the indicated inhibitors migrating in a collagen-I matrix in response to CCL21. Scale bar: 100 µm. (**F, G**) Mean (±95% CI) speed of mouse naive CD4$^+$ T cells of the indicated genotypes or treated with inhibitors migrating in a collagen-I matrix in response to CCL21. 3 mice (C), and ≥422 (D), ≥188 (F) and ≥491 (G) cells per condition. Data pooled from at least 3 (C) or 2 (F, G) independent experiments or from one experiment representative of 2 independent experiments (D). Statistical analysis was carried using 2-way ANOVA (C), Mann-Whitney (F) or 1-way ANOVA (G); n.s., not significant, *$0.01 < q < 0.05$, ***$0.0001 < q < 0.001$, ****p or $q < 0.0001$.

Figure S2

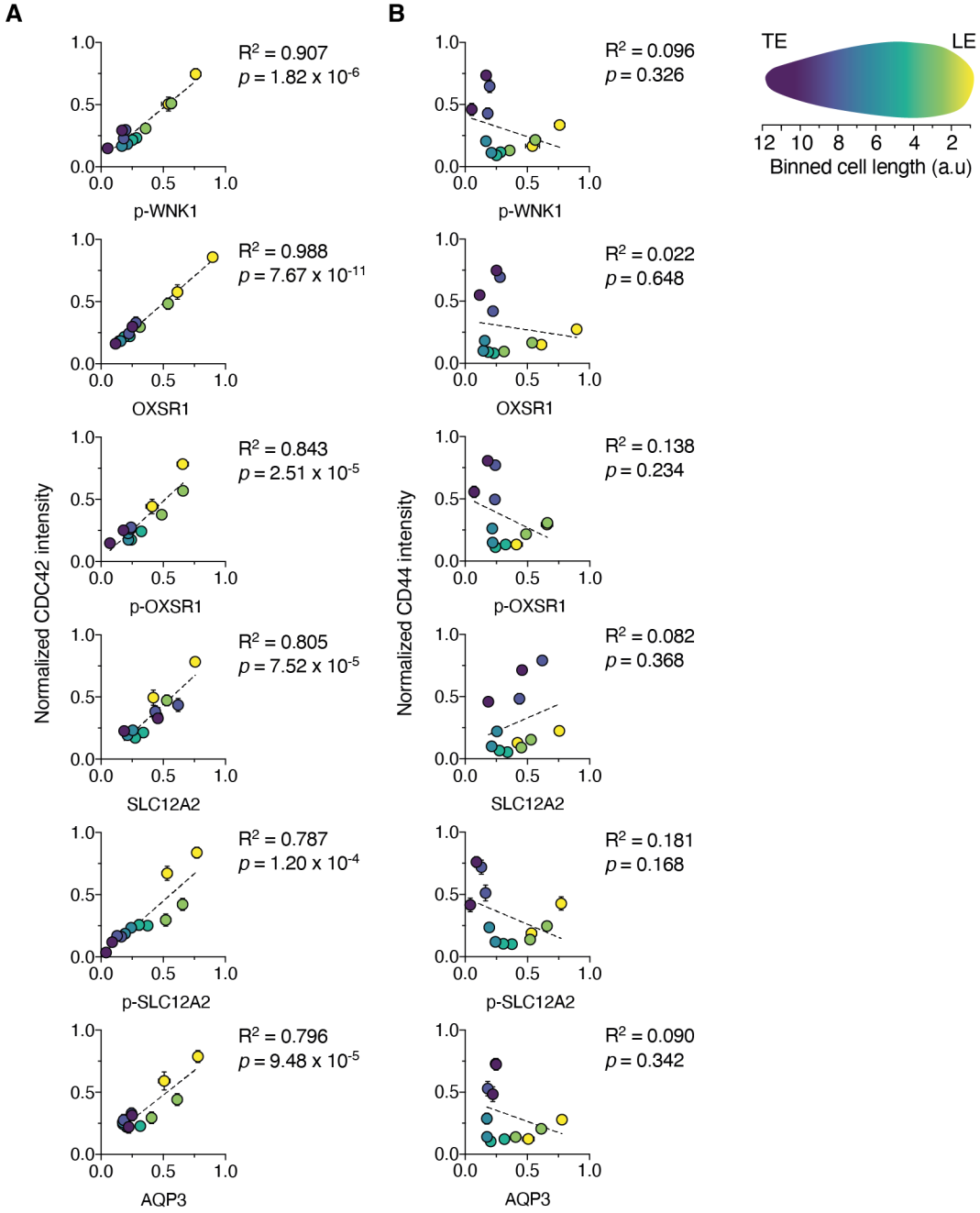

Figure S2. WNK1 pathway proteins polarize to the leading edge of migrating CD4$^+$ T cells.

(**A, B**) Mouse naïve CD4$^+$ T cells migrating in response to CCL21 on ICAM-1 were fixed and stained with antibodies against the indicated proteins. Graphs show normalized fluorescence intensity of p-WNK1, OXSR1, p-OXSR1, SLC12A2, p-SLC12A2 and AQP3 versus the normalized fluorescence intensity of CDC42 (A) or

CD44 (B), markers of the leading and trailing edges of the cell, respectively. Dots represent the mean (±SEM) fluorescence intensity, at different positions along the length of the cell as indicated by the colors representing 12 bins from the leading to the trailing edge (see legend). This is the same data that is shown in Figure 2E. LE, leading edge, TE, trailing edge, a.u., arbitrary units. ≥ 47 cells pooled from at least 2 experiments per protein. *p*-values determined using Pearson's correlation test; R, correlation coefficient.

Figure S3

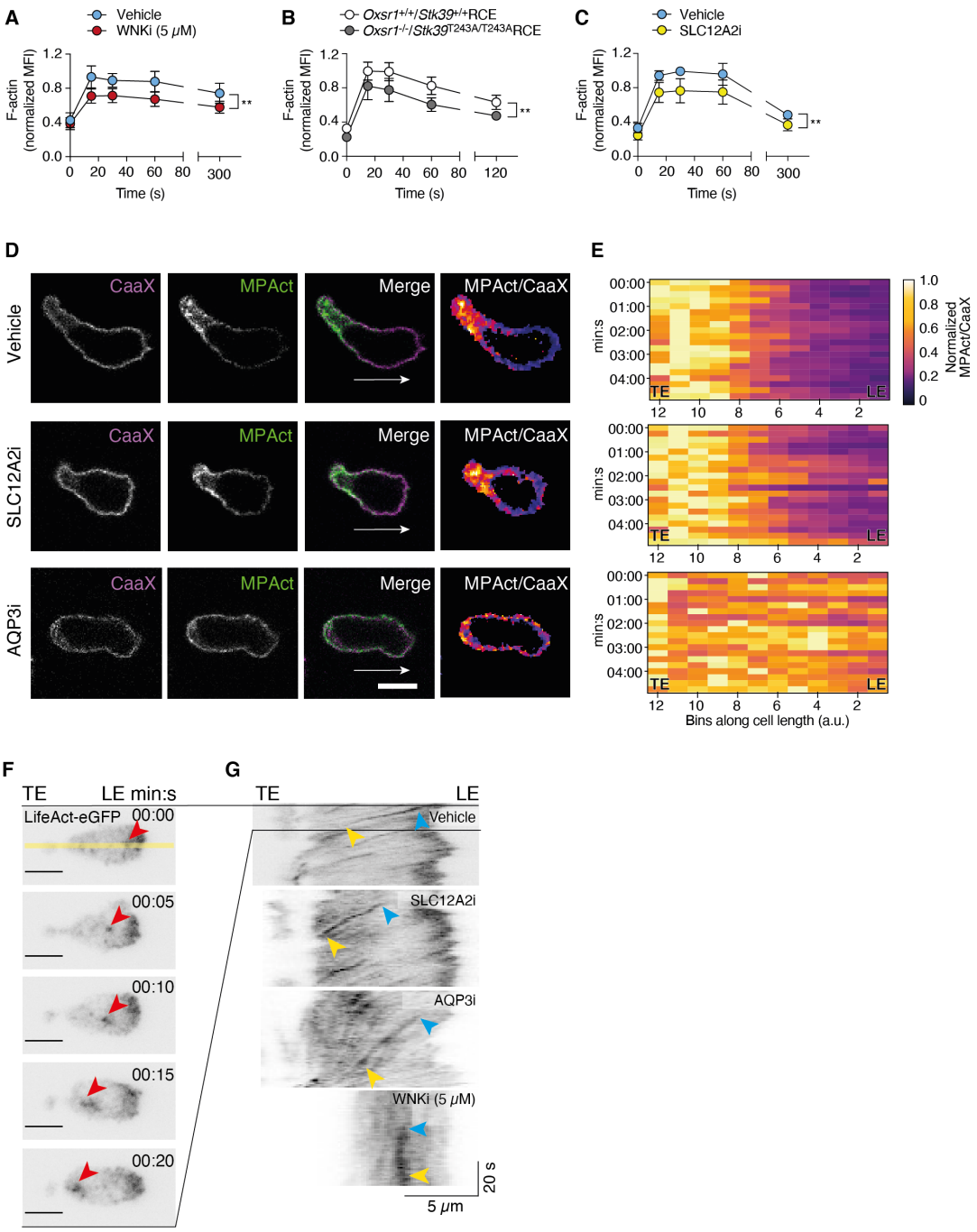

Figure S3. The WNK1 pathway regulates F-actin in migrating CD4⁺ T cells.

(**A-C**) Mean (±95% CI) F-actin in naïve CD4⁺ T cells of the indicated genotypes or treated with inhibitor or vehicle, stimulated with CCL21 for the indicated times and measured by flow cytometry. (**D, E**) Mouse naïve CD4⁺ T cells co-expressing GFP-CaaX (CaaX) and MPAct-mCherry (MPAct), were imaged migrating in response to CCL21 on ICAM-1 under agarose in the presence of inhibitors or vehicle. Cells were

imaged every 15 s, for 2.5 or 5 min. Representative images of CaaX and MPAct fluorescence and MPAct/CaaX ratio in cells treated with vehicle or inhibitors showing direction of migration (white arrow); scale bar, 5 μm (D). Heatmaps showing normalized MPAct/CaaX ratios over time of the three cells shown in C (E). LE, leading edge; TE, trailing edge. (**F, G**) Total internal reflection fluorescence microscopy of mouse naive $CD4^+$ T cells expressing LifeAct-eGFP migrating on PEG-coated glass under agarose in response to CCL21, treated with inhibitors or vehicle only. LifeAct-eGFP fluorescence was imaged every 1 s for 1 min. Images of vehicle-treated cells at a series of timepoints showing retrograde movement of F-actin (red arrowhead); scale bars, 5 μm (F). Yellow line indicates location of line used for kymograph generation. Representative kymographs of mouse naïve $CD4^+$ T cells treated with vehicle or inhibitors derived from time-lapse imaging as shown in F, taking fluorescence along the length of the cell (G). The top kymograph is taken from the cell in F, blue and yellow arrowheads indicate the start and end of F-actin flow respectively, the slope of the time-dependent F-actin flow was used to calculate the retrograde actin flow rates shown in Figure 4F, G, J. ≥5 mice at each timepoint (A-C). Data are pooled from at least 2 experiments. 2-way ANOVA (A-B), mixed-effects model (C) with FDR correction; $^{**}0.001 < q < 0.01$.

Supplementary Videos

Video S1. CD4$^+$ T cell migration under agarose.

Widefield microscopy of CTV-labelled *Wnk1*$^{+/-}$RCE or *Wnk1*$^{-/-}$RCE naïve CD4$^+$ T cells, stimulated with CCL21, migrating under agarose on an ICAM-1 coated dish for 10 min, imaged every 15s. Purple, CTV labelled cells; yellow, propidium iodide for dead cell exclusion. Time stamp: min:s. Scale bar, 200 µm.

Video S2. CD4$^+$ T cell migration in a collagen-I matrix.

Z-projected confocal microscopy of CTV-labelled mouse naïve CD4 T cells from C57BL/6J mice suspended in a collagen-I matrix, stimulated with CCL21 in the presence of the indicated inhibitors, or vehicle only. Cells were imaged every 15 s for 10 min, in a 120 µm z-stack. Black, CTV labelled cells; red, propidium iodide for dead cell exclusion. Time stamp: min:s. Scale bar, 100 µm.

Video S3. GFP-tagged WNK1 pathway proteins in migrating CD4$^+$ T cells.

Confocal microscopy of CD4$^+$ T cells expressing GFP-WNK1, GFP-OXSR1, GFP-SLC21A2 or GFP only migrating on ICAM-1 under agarose in response to CCL21. Cells were imaged every 15 s for 2.5 min. Look-up table GFP intensity: yellow, high; blue-black, low. Time stamp: min:s. Scale bar, 5 µm.

Video S4. Plasma membrane-F-actin spacing in migrating CD4$^+$ T cells.

iSIM imaging of mouse naïve CD4$^+$ T cells expressing LifeAct-eGFP (cyan) migrating on ICAM-1 under agarose in response to CCL21, treated with inhibitors or vehicle only. To visualize the plasma membrane, cells were labelled with CellMask Orange plasma membrane stain (magenta). Images were taken every 250 ms. Time stamp: s:ms. Scale bar, 5 µm.

Video S5. Membrane-proximal F-actin in migrating CD4$^+$ T cells.

Confocal microscopy of naive CD4$^+$ T cells expressing MPAct-mCherry and GFP-CaaX migrating on ICAM-1 under agarose in response to CCL21, treated with inhibitors or vehicle only. Fluorescence was imaged every 15 s for 2.5 min. Look-up table of MPAct/CaaX ratio intensity: yellow, high; blue-black, low (as in Fig. 4A). Time stamp: min:s. Scale bar, 5 μm.

Video S6. Actin retrograde flow in migrating CD4$^+$ T cells.

CD4$^+$ T cells expressing LifeAct-eGFP migrating on PEG-coated glass under agarose in response to CCL21, treated with inhibitors or vehicle only, imaged by TIRF microscopy. LifeAct-eGFP fluorescence was imaged every 1 s for 1 min. Black, LifeAct-eGFP. Time stamp: s. Scale bar, 5 μm.